

Leveraging Locality to Boost Sample Efficiency in Robotic Manipulation

Tong Zhang^{1,2,3} Yingdong Hu^{1,2,3} Jiacheng You¹ Yang Gao^{1,2,3*}

¹Tsinghua University ²Shanghai Artificial Intelligence Laboratory ³Shanghai Qi Zhi Institute
{zhangton20,huyd21,yjc23}@mails.tsinghua.edu.cn, gaoyangiiis@mail.tsinghua.edu.cn

Abstract: Given the high cost of collecting robotic data in the real world, sample efficiency is a consistently compelling pursuit in robotics. In this paper, we introduce SGRv2, an imitation learning framework that enhances sample efficiency through improved visual and action representations. Central to the design of SGRv2 is the incorporation of a critical inductive bias—*action locality*, which posits that robot’s actions are predominantly influenced by the target object and its interactions with the local environment. Extensive experiments in both simulated and real-world settings demonstrate that action locality is essential for boosting sample efficiency. SGRv2 excels in RL Bench tasks with keyframe control using merely 5 demonstrations and surpasses the RVT baseline in 23 of 26 tasks. Furthermore, when evaluated on ManiSkill2 and MimicGen using dense control, SGRv2’s success rate is 2.54 times that of SGR. In real-world environments, with only eight demonstrations, SGRv2 can perform a variety of tasks at a markedly higher success rate compared to baseline models. Project website: sgrv2-robot.github.io.

Keywords: Robotic Manipulation, Sample Efficiency

1 Introduction

The creation of a versatile, general-purpose robot has long captivated the robotics community. Recent advances in imitation learning (IL) [1, 2, 3] have enabled robots to exhibit increasingly complex manipulation skills in unstructured environments. However, prevailing imitation learning techniques frequently require an abundance of high-quality demonstrations, the acquisition of which incurs substantial costs. This contrasts markedly with disciplines such as computer vision (CV) and natural language processing (NLP), wherein vast repositories of internet data are readily available for utilization. In this paper, we investigate methods to boost **sample efficiency** in robotic manipulation by developing improved visual and action representations.

In machine learning, introducing inductive bias is a standard strategy to enhance sample efficiency. For instance, CNNs [4, 5] inherently embed spatial hierarchies and translation equivariance in each layer, while RNNs [6] and LSTMs [7] incorporate temporal dependencies in their architecture. In the realm of robotic manipulation, a critical inductive bias is **action locality**, which posits that a robot’s actions are predominantly determined by the target object and its relationship with the surrounding local environment. However, previous studies on representation learning for robotic manipulation have not effectively leveraged this bias. Typically, these studies [8, 9, 10, 11] aim to develop a global representation that encapsulates the entire scene, which is then directly employed to predict robot actions. These approaches have demonstrated notably low sample efficiency. As depicted in Figure 1, reducing the number of demonstrations from 100 to 5 leads to a substantial decrease in the performance of previous works such as SGR [10], which seeks to capture both semantic and geometric information in a global vector.

*Corresponding author

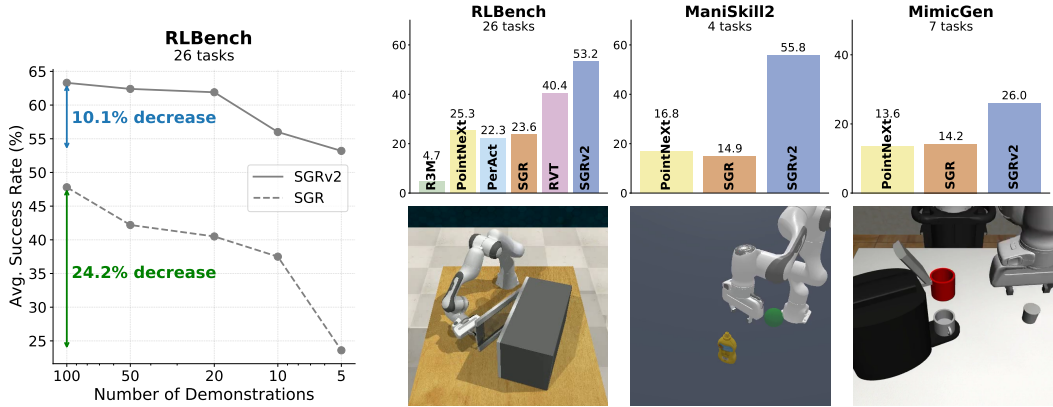


Figure 1: **Left:** Sample efficiency of SGRv2. We evaluate SGR and SGRv2 on 26 RL Bench tasks, with demonstration numbers ranging from 100 to 5. Results indicate that, owing to the locality of SGRv2, it exhibits exceptional sample efficiency, with its success rate declining by only about 10%. **Top Right:** Overview of simulation results. We test SGRv2 on 3 benchmarks, consistently outperforming the baselines. **Bottom Right:** Tasks of the 3 simulation benchmarks.

To effectively utilize the inductive bias of action locality, we introduce SGRv2, a systematic framework of visuomotor policy that considers both visual and action representations. As shown in Figure 2, SGRv2 builds on the foundation of SGR but integrates action locality throughout the entire framework. SGRv2 demonstrates exceptional sample efficiency and consistently outperforms its predecessor across various demonstration sizes, achieving remarkable results with as few as 5 demonstrations, compared to SGR’s performance with 100 demonstrations. The key algorithmic designs that lead to this achievement include: (i) an encoder-decoder architecture for extracting point-wise features, (ii) a strategy for predicting the *relative* target position to ensure translation equivariance, (iii) the application of point-wise weights to highlight critical local regions, and (iv) dense supervision to enhance learning efficiency.

We conduct an extensive evaluation of SGRv2 through behavior cloning across three benchmarks: RLBench [12], where keyframe control is utilized, and ManiSkill2 [13] and MimicGen [14], where dense control is applied (refer to Section 3.1 for a discussion on keyframe versus dense control). SGRv2 significantly surpasses both SGR [10] and PointNeXt [15] across these benchmarks and consistently outperforms baselines, including R3M [9], PerAct [16], and RVT [17] on RLBench. To confirm the necessity of our locality design, we conduct a series of ablation studies. Additionally, real-world experiments with Franka Emika Panda robot demonstrate SGRv2’s capability to complete complex long-horizon tasks across 10 sub-tasks, validating its effectiveness. Further experiments on real-world generalization underscore SGRv2’s remarkable ability to generalize.

2 Related Work

Semantic Representation Learning for Robotics. Numerous studies have focused on learning visual representations from *in-domain* data, tailored specifically to the relevant environment and task [18, 19, 20, 21, 22, 23, 24]. However, the efficacy of these methods is limited by the availability of robot data. Consequently, various efforts have been made to pre-train on large-scale *out-of-domain* data for visuo-motor control [25, 26, 27, 8, 28, 29, 30, 31]. Notably, R3M [9] has demonstrated that models pre-trained on human video data can serve as a frozen perception module, facilitating downstream policy learning. Nonetheless, these approaches predominantly prioritize the pre-training of 2D visual representations, thus overlooking critical 3D geometric information, which is essential for enhancing spatial manipulation skills in robotics.

3D Representation Learning for Robotics. Recent works have increasingly explored the 3D representations in robotics. Studies such as C2F-ARM [32], PerAct [16], and GNFactor [33] employ voxelized observations to derive representations. However, the creation and reasoning over voxels entail a high computational burden. In contrast, RVT [17] and some researches [34, 35, 36] lever-

age projection techniques to generate multi-view images, extracting representation in 2D spaces and thereby reducing computational demands. Nevertheless, these methods do not incorporate 3D geometry in the process of representation extraction, consequently limiting their capacity for 3D spatial reasoning. Point-based models, such as PointNet++ [37] and PointNeXt [15], efficiently conserve computational resources while directly processing 3D information. These models serve as the foundation for numerous robotics studies [38, 39, 40, 41, 42, 43, 44, 45, 46]. Specifically, SGR [10] utilizes point-based models to extract 3D geometric information and employs 2D foundational models for semantic understanding, integrating both to enrich representations for downstream tasks. However, the approach of SGR to extract actions from a global vector does not effectively harness locality information, thereby leading to suboptimal sample efficiency.

Incorporating Inductive Biases into Robot Learning. Incorporating inductive biases is an essential strategy for enhancing sample efficiency in neural network designs. Several studies have sought to improve sample efficiency by designing networks that adhere to *equivariance* properties. For example, Act3D [44] employs a translation-equivariant neural network architecture, while USEEK [47] utilizes an SE(3)-equivariant keypoint detector for one-shot imitation learning. However, these approaches are based on global equivariance [48], which may not be effective when there are relative movements between the object and the environment, which is prevalent in robot manipulation. To tackle this issue, NDFs [49] and EquivAct [50] segment the manipulated object before utilizing the equivariant models. However, given their reliance on a well-segmented point cloud, these methods are ineffective when the object is required to interact with its surroundings.

Some studies integrate *locality* into their models. L-NDF [51] incorporates locality through voxel partitioning, EDFs [48] and RiEMann [52] achieves both equivariance and locality via local message-passing mechanisms in SE(3)-Transformers [53]. Nonetheless, these methods require some hyperparameters to specify a proper size of receptive field, which limits their flexibility and extensibility. It also incurs a tradeoff between locality and expressiveness. Another line of work, such as Transporter [54], PerAct [16], and RVT [17], integrates locality by modeling action as the maximizer of scores on a predefined grid of locations. However, these designs render a voluminous action representation and suffer from quantization artifacts [55]. In contrast, our approach not only satisfies translation equivariance without relying on highly non-local centroid subtraction [49, 56] but also adaptively determines the local scope required for the task through a learnable weight, without sacrificing expressiveness or introducing a grid.

3 Method

In this section, we present a detailed description of the methodologies employed in SGRv2. Initially, we present an overview of SGR, keyframe and dense control, along with the problem formulation, as outlined in Section 3.1. Subsequently, we explore how to leverage the inductive bias of locality to enhance sample efficiency in robotic manipulation learning, as discussed in Section 3.2. Finally, we describe the training approaches under different control modes, detailed in Section 3.3.

3.1 Background

Semantic-Geometric Representation (SGR) [10]. SGR is composed of the semantic branch, geometric branch and fusion network. In the semantic branch, the RGB part of RGB-D images are fed into a CLIP [57] image encoder, and the resulting semantic features are then back-projected onto the 3D points. The geometric branch and fusion network split a PointNeXt encoder into two stages, with semantic features injected at the interface between them. SGR models the action by solely relying on the global features extracted by the PointNeXt [15] encoder, without utilizing locality.

Keyframe and Dense Control. In the field of robotic manipulation, keyframe control [32, 16, 58] and dense control [13, 59] are two prevalent control modes. Keyframe control outputs a few sparse target poses, which are then executed through a motion planner. It exhibits reduced compounding errors [58], and enhanced suitability for visuomotor tasks that leverage visual priors [32, 16, 17] at the cost of inferior flexibility and expressiveness. Dense control, on the other hand, generates a

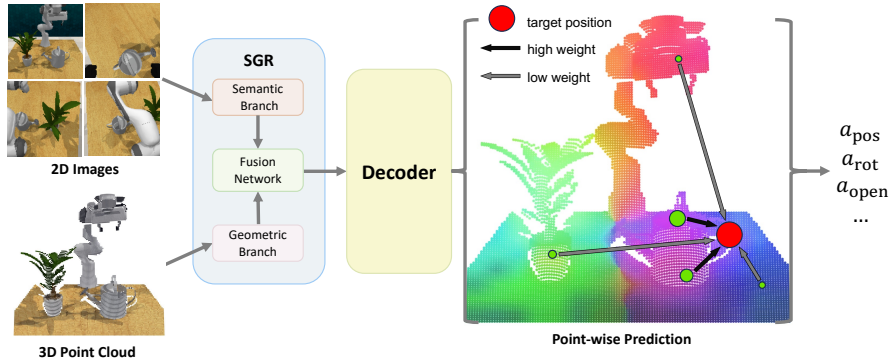


Figure 2: **SGRv2 Architecture.** Built upon SGR, SGRv2 integrates locality into its framework through four primary designs: an encoder-decoder architecture for point-wise features, a strategy for predicting relative target position, a weighted average for focusing on critical local regions, and a dense supervision strategy (not shown in the figure). For simplicity in the visualization, we omit the proprioceptive data that is concatenated with the RGB of the point cloud before being fed into the geometric branch.

dense sequence with hundreds of actions to control the robot directly. It is applicable across a wide range of robotic scenarios but faces significant challenges with compounding errors. Given that the two models are complementary, it is highly compelling to construct a framework that supports both simultaneously. However, previous research has predominantly focused on a single control mode [16, 17, 60]. In contrast, our framework can support both modes seamlessly.

Problem Formulation. We frame our task as a vision-based robot manipulation problem. At each timestep, the robot receives an observation O comprising single or multi-view RGB-D images $\{I_k\}_{k=1}^K$ and proprioceptive data z . For keyframe control, following the setup in PerAct [16], an action consists of the position, rotation, gripper open state, and collision indicator: $a^{\text{keyframe}} = \{a_{\text{pos}}, a_{\text{rot}}, a_{\text{open}}, a_{\text{collide}}\}$. For dense actions, as illustrated in ManiSkill2 [13] and robosuite[59], an action consists of the delta position, delta rotation, and gripper open state [13, 59, 14]: $a^{\text{dense}} = \{a_{\Delta\text{pos}}, a_{\Delta\text{rot}}, a_{\text{open}}\}$. We assume we are given N expert demonstration trajectories $D = \{\tau_i\}_{i=1}^N$. Each trajectory τ_i is a sequence of observation-action pairs $(o_1, a_1, \dots, a_{T-1}, o_T)$. The robot is then trained using the Behavioral Cloning (BC) algorithm with these demonstrations.

3.2 Locality Aware Action Modeling

To develop a sample-efficient framework for robotic manipulation that is effective in both keyframe and dense control scenarios, we capitalize on the inductive bias that actions exhibit locality properties and build our locality aware action modeling on the top of SGR. In SGRv2, we achieve locality through 4 primary designs: (1) an encoder-decoder architecture, (2) a strategy for predicting point-wise relative position formulation with (3) a learned weight, and (4) a dense supervision strategy. Refer to Figure 2 for an overview of our designs and Table 3 for ablation studies.

Encoder-Decoder Architecture. In contrast to the encoder-only architecture used by SGR [10], we employ the encoder-decoder architecture of PointNeXt [15], which is a U-Net like architecture that excels in dense prediction tasks (e.g. segmentation). This architecture can yield a feature enriched with both global and local information for each point, namely $f_i \in \mathbb{R}^C$ for the i -th point, where C is the dimension of the feature. Note that as designed in PointNeXt [15], the output features are solely dependent on *relative* coordinates, ensuring that the point-wise features f_i remain invariant to translational transformations of the input coordinates. This point-wise features serve as the cornerstone of our locality aware action modeling.

Relative Position Predictions. With the point-wise features, we can predict an action at each point. Our key insight is that the end-effector usually moves towards a target close to a specific object within each execution stage. Thus, it is natural to predict the displacement of the target relative to each point. Driven by this insight, for *keyframe*, we represent the position component of a *keyframe* action a_{pos} by $p_i + \Delta p(f_i)$ for the i -th point, where p_i and f_i are the coordinate and point-wise feature of the i -th point respectively, and Δp is a Multilayer Perceptrons (MLP). For *dense* control, we can predict the delta position component $a_{\Delta\text{pos}}$ of a *dense* action by modeling its direction (towards a

target) and magnitude separately. Concretely, we predict the direction $\frac{a_{\Delta\text{pos}}}{\|a_{\Delta\text{pos}}\|_2}$ by $\frac{p_i + \Delta p(f_i)}{\|p_i + \Delta p(f_i)\|_2}$ and the magnitude $\|a_{\Delta\text{pos}}\|_2$ by $m(f_i)$, where m is another MLP. In dense control, given that we employ the end-effector coordinate frame for the point cloud input², $p_i + \Delta p(f_i)$ can be interpreted as the target position relative to the end-effector. Consequently, $\frac{p_i + \Delta p(f_i)}{\|p_i + \Delta p(f_i)\|_2}$ can represent the direction of movement. The utilization of relative position leverages the locality information and achieves translation equivariance without depending on the extensive non-local centroid subtraction [49, 56]. This greatly aids in enhancing sample efficiency.

For other action components, we directly predict rotation by $r(f_i)$, gripper open state by $o(f_i)$ and collision indicator by $c(f_i)$, where r, o, c are MLPs.

Weighted Average Actions. After obtaining the point-wise action predictions, we need to integrate these predictions into an aggregated action prediction. We adopt a simple yet effective strategy, namely weighted average. For each component, including position (which is broken down into direction and magnitude in dense control), rotation, gripper open state, and collision indicators, we employ a learned weight $w_*(f_i)$ for each point. Here, w_* denotes separate MLPs (softmax is applied for normalization) for each component. The motivation behind this design is that only a few regions within the point cloud are crucial for accomplishing the task. For instance, in tasks such as picking up a cube, points located on the cube itself are more informative than those on the surrounding table. By learning these weights, we enable the aggregated prediction to concentrate on the most predictive local regions, thereby enhancing both the overall accuracy and sample efficiency.

Dense Supervision. To enhance the learning efficiency of local features, we adopt a dense supervision strategy. This approach integrates both aggregated action predictions and point-wise action predictions into the loss function, expressed as $\mathcal{L}_* = \mathcal{L}_*^{\text{aggregated}} + \mathcal{L}_*^{\text{points}}$. To compute $\mathcal{L}_*^{\text{aggregated}}$ and $\mathcal{L}_*^{\text{points}}$, we adopt the same loss formulation with the same ground-truth labels. Dense supervision provides feedback for all points, enabling models to learn local features more efficiently.

3.3 Training

Smoothness Regularization for Dense Control. As illustrated in point-wise relative predictions, we predict the direction and the magnitude of the delta position component $a_{\Delta\text{pos}}$ separately. Thus, the position loss is accordingly decomposed into \mathcal{L}_{dir} and \mathcal{L}_{mag} , i.e. $\mathcal{L}_{\text{pos}} = \mathcal{L}_{\text{dir}} + \mathcal{L}_{\text{mag}}$. We predict the direction by $\frac{p_i + \Delta p(f_i)}{\|p_i + \Delta p(f_i)\|_2}$, which poses an underdetermined problem and allows Δp to output spuriously large values. To mitigate this issue, we incorporate a smoothness regularization loss $\mathcal{L}_{\text{reg}} = \frac{1}{N^2} \sum_{i,j} \|(p_i + \Delta p(f_i)) - (p_j + \Delta p(f_j))\|_2^2$. This loss enforces the consistency between $p_i + \Delta p(f_i)$ and $p_j + \Delta p(f_j)$ for any two points i and j .

Overview of Losses. In keyframe control, following SGR [10], position is represented by a continuous 3D vector: $a_{\text{pos}} \in \mathbb{R}^3$. For rotations, the ground-truth action is represented as a one-hot vector per rotation axis with R rotation bins: $a_{\text{rot}} \in \mathbb{R}^{(360/R) \times 3}$ ($R = 5$ degrees in our implementation). Open and collide actions are binary one-hot vectors: $a_{\text{open}} \in \mathbb{R}^2, a_{\text{collide}} \in \mathbb{R}^2$. In this way, our loss objective is as follows:

$$\mathcal{L}_{\text{keyframe}} = \alpha_1 \mathcal{L}_{\text{pos}} + \alpha_2 \mathcal{L}_{\text{rot}} + \alpha_3 \mathcal{L}_{\text{open}} + \alpha_4 \mathcal{L}_{\text{collide}}, \quad (1)$$

where \mathcal{L}_{pos} is L1 loss, and $\mathcal{L}_{\text{rot}}, \mathcal{L}_{\text{open}},$ and $\mathcal{L}_{\text{collide}}$ are cross-entropy losses.

In dense control, following ManiSkill2 [13] and robosuite [59], both delta position and delta rotation (in the form of axis-angle coordinates) are represented by continuous 3D vectors: $a_{\Delta\text{pos}} \in \mathbb{R}^3, a_{\Delta\text{rot}} \in \mathbb{R}^3$, while open actions are still binary one-hot vectors: $a_{\text{open}} \in \mathbb{R}^2$. Our loss objective is:

$$\mathcal{L}_{\text{dense}} = \beta_1 (\mathcal{L}_{\text{dir}} + \mathcal{L}_{\text{mag}}) + \beta_2 \mathcal{L}_{\text{rot}} + \beta_3 \mathcal{L}_{\text{open}} + \beta_4 \mathcal{L}_{\text{reg}}, \quad (2)$$

where $\mathcal{L}_{\text{dir}}, \mathcal{L}_{\text{mag}}$ and \mathcal{L}_{rot} are MSE losses, $\mathcal{L}_{\text{open}}$ is cross-entropy loss, and \mathcal{L}_{reg} is smoothness regularization loss. For more training details, we refer to Appendix B.

²Motivated by FrameMiner [43], in dense control, we transform the point coordinates into the end-effector frame, positioning the end-effector at the origin of coordinates for easier computation and performance benefit.

Method	Avg. Success \uparrow	Avg. Rank \downarrow	Open Microwave	Open Door	Water Plants	Toilet Seat Up	Phone On Base	Put Books	Take Out Umbrella	Open Fridge	Open Drawer	Slide Block	Sweep To Dustpan	Meat Off Grill
R3M	4.7	5.8	0.9	36.4	2.9	15.5	0.0	0.5	5.2	3.2	0.0	24.0	0.4	0.1
PointNeXt	25.3	3.4	7.1	60.9	5.6	49.9	46.4	57.5	37.5	9.2	21.7	59.5	42.0	59.9
PerAct	22.3	4.1	4.3	59.6	28.5	69.3	0.0	25.1	75.9	3.1	56.4	47.5	2.8	85.9
SGR	23.6	4.1	6.4	55.3	24.9	30.7	47.2	29.3	36.3	7.1	31.9	72.0	43.6	52.7
RVT	40.4	2.2	18.3	71.2	34.8	47.6	62.3	46.5	85.3	24.0	75.1	85.1	19.6	90.5
SGRv2 (ours)	53.2	1.2	27.2	76.8	38.0	89.6	84.1	63.7	74.5	13.2	81.3	100.0	61.5	96.5

Method	Turn Tap	Put In Drawer	Close Jar	Drag Stick	Stack Blocks	Screw Bulb	Put In Safe	Place Wine	Put In Cupboard	Sort Shape	Push Buttons	Insert Peg	Stack Cups	Place Cups
R3M	26.1	0.0	0.0	0.3	0.0	0.0	0.3	0.4	0.0	0.0	6.8	0.0	0.0	0.0
PointNeXt	48.7	17.1	36.0	18.5	1.9	4.1	12.1	31.5	3.3	0.4	22.0	0.1	4.4	0.4
PerAct	8.0	0.1	0.5	10.3	1.7	4.4	0.9	8.7	0.4	0.4	83.1	1.9	0.1	0.7
SGR	34.4	8.3	13.3	64.4	0.0	0.9	16.9	24.7	0.1	0.1	12.0	0.1	0.0	1.1
RVT	38.4	19.6	25.2	45.7	8.8	24.0	30.7	92.7	5.6	1.6	90.4	4.0	3.1	1.2
SGRv2 (ours)	87.9	75.9	25.6	94.9	17.5	24.1	55.6	53.1	20.3	1.9	93.2	4.1	21.3	1.6

Table 1: **Performance on RL Bench with 5 Demonstrations.** All numbers represent percentage success rates averaged over 3 seeds. See Appendix D for standard deviation. SGRv2 outperforms the most competitive baseline RVT on 23/26 tasks, with an average improvement of 1.32 \times .

4 Experiments

Our experiments are designed to answer the following questions: (1) How does SGRv2 perform when locality is incorporated into designs, especially in data-limited scenarios, compared to various 2D and 3D representations? (2) Can SGRv2 consistently demonstrate advantages across different control modes? (3) What are the contributions of the key components of SGRv2’s locality design to its overall performance? (4) How does SGRv2 perform in real-robot tasks, and does it possess the ability to generalize in the real world?

4.1 Simulation Setup

Environment and Tasks. The simulation experiments are conducted on 3 robot learning benchmarks: RL Bench [12], ManiSkill2 [13], and MimicGen [14]. RL Bench is a large-scale benchmark designed for vision-guided manipulation. Following previous works [32, 16, 17] we use keyframe control on RL Bench. ManiSkill2 is a comprehensive benchmark for manipulation skills, enhancing diversity with object-level variations. MimicGen generates large-scale robot learning datasets from human demonstrations. On ManiSkill2 and MimicGen, following prior works [60, 14], we use dense control. On RL Bench, we use 4 RGB-D cameras positioned at the front, left shoulder, right shoulder, and wrist of a Franka Emika Panda, while on ManiSkill2 and MimicGen, we use a front-view and a wrist-view RGB-D camera. We use 26 RL Bench tasks with 5 demonstrations per task, and 4 ManiSkill2 tasks and 7 MimicGen tasks with 50 demonstrations per task (except for *PickSingleYCB*, where 50 demonstrations per object are used). On MimicGen, we use D_1 initial distribution, which presents a broader and more challenging range. See Appendix A for more details.

Evaluation. The evaluation approach is carefully designed to minimize variance in our results. On RL Bench, we train an agent for 20,000 iterations and save checkpoints every 800 iterations, while in ManiSkill2 and MimicGen, we train for 100,000 iterations and save checkpoints every 4,000 iterations. Then we evaluate the last 5 checkpoints for 50 episodes and get the average success rates. Finally, we conduct the experiments with 3 seeds and report the average results.

Baselines. We compare SGRv2 against the following baselines: (1) **R3M** [9] is a 2D visual representation designed for robotic manipulation, which is pre-trained on large-scale human video datasets. For fair comparisons, we utilize frozen R3M to process RGB images, employ a separate 2D CNN to process depth images, and subsequently fuse the two resulting features. (2) **PointNeXt** [15] is an enhanced version of the classic PointNet++ architecture for point cloud processing. We employ the encoder of PointNeXt to obtain the 3D representation. (3) **PerAct** [16] is a 3D representation that voxelizes the workspace and utilizes a Perceiver Transformer [61] to process voxelized observations. (4) **SGR** [10] is a representation that integrates both high-level 2D semantic understanding and low-level 3D spatial reasoning. (5) **RVT** [17] is a 3D representation that utilizes a multi-view transformer to predict actions and integrates these predictions into a 3D space through back-projection from multiple viewpoints.

Method	Avg. Success \uparrow	Avg. Rank \downarrow	LiftCube	PickCube	StackCube	PickSingleYCB
PointNeXt	16.8	2.5	50.8	4.7	10.6	1.1
SGR	14.9	2.5	26.9	12.2	3.5	17.0
SGRv2 (ours)	55.8	1.0	80.5	72.9	27.7	42.2

Method	Avg. Success \uparrow	Avg. Rank \downarrow	Stack	StackThree	Square	Threading	Coffee	HammerCleanup	MugCleanup
PointNeXt	13.6	2.9	56.1	3.7	0.9	3.6	12.0	11.7	7.1
SGR	14.2	2.0	50.8	5.6	1.3	4.0	14.1	14.1	9.7
SGRv2 (ours)	26.0	1.0	81.2	37.9	2.8	6.7	27.9	16.1	9.7

Table 2: **Performance on ManiSkill2 (top) and MimicGen (bottom) with 50 Demonstrations.** We report success rates averaged over 3 seeds. We observe that SGRv2 consistently outperforms baselines like SGR and PointNeXt.

4.2 Simulation Results

RLBench Performance. Figure 1 depicts the performance of SGR and SGRv2 across differing number of demonstrations. Initially, as the availability of data decreases, we note a significant decline in SGR’s performance compared to SGRv2, highlighting the difficulties in maintaining model performances without the inductive bias towards locality awareness. Additionally, Table 1 provides a comparison of success rates obtained with only 5 demonstrations using various representations. We observe that the absence of 3D geometric information, as demonstrated by R3M using a 2D representation, results in markedly low performance, highlighting the critical role of 3D priors in robotic manipulation under data-constrained scenarios. Finally, SGRv2 is demonstrated to be the superior representation, achieving 53.2% average success rate with merely 5 demonstrations and significantly outperforming the most competitive baseline, RVT, with an average improvement factor of $1.32\times$ and achieving enhanced performance in 23 out of 26 tasks. The results underscore the advantages of incorporating 3D geometry and well-designed locality to enhance sample efficiency.

ManiSkill2 and MimicGen Performance. To evaluate the performance of SGRv2 in dense control scenarios, we conduct comparisons with several baselines on ManiSkill2 and MimicGen. Our experimental results, summarized in Table 2, demonstrate that SGRv2 significantly outperforms the baselines. In particular, thanks to our tailored approach for dense control, SGRv2 exhibits superior performance in tasks where the object’s location consistently aligns with the direction of the delta actions, such as *Pick Cube* and *Stack Three*. These findings confirm that SGRv2 acts as a sample-efficient, universal representation adept at handling both keyframe and dense control scenarios.

Ablations. As shown in Table 3, we conduct ablations to assess the locality design choices of SGRv2. (1) Decoder architecture is the cornerstone of our locality designs. Omitting the decoder from the SGRv2 would prevent the application of other locality designs, forcing us to rely solely on the global representation from the encoder. This would lead to a significant decrease in performance. (2) Predicting absolute positions, results in markedly poorer performance. This underscores that relative position predictions are the key insight of the locality design. (3) Substituting point-wise weights with uniform weights reduces performance, confirming the role of point-wise weighting in focusing on predictive local regions. (4) Eliminating dense supervision leads to a decline in overall performance, illustrating that dense supervision enhances the model’s learning efficacy.

Method	Avg. success
SGRv2	53.2
SGRv2 w/o decoder	21.3
SGRv2 w/ absolute pos prediction	21.0
SGRv2 w/ uniform point weight	44.2
SGRv2 w/o dense supervision	40.0

Table 3: **Ablations.** Average success rate of 26 RLBench tasks with 5 demonstrations after ablating key components of locality design.

Emergent Capabilities. In our study, we conduct a visualization of point-wise weights of SGRv2 detailed in Section 3.2. As depicted in Figure 3, we sequentially visualize point clouds with RGB and point-wise weights. Surprisingly, our visualizations consistently demonstrate an alignment between points with higher weights (marked in red) and the object affordances, which denote the functional areas of objects. This observation highlights the capability of our method to precisely identify and emphasize critical local regions on objects.

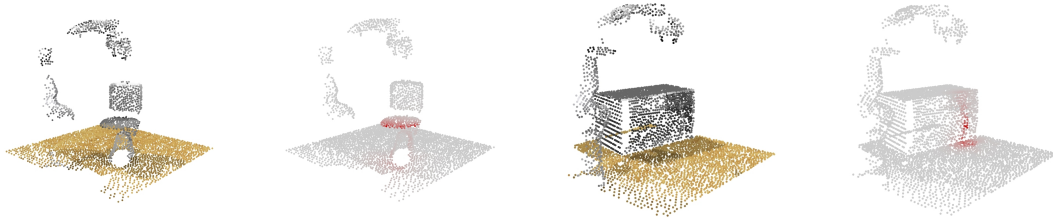


Figure 3: **Emergent Capabilities by SGRv2.** We visualize the point-specific weights and unexpectedly discover that the points with high weights (indicated by the red points) align with the object’s affordances.



Task	Sub-task	PerAct	RVT	SGRv2
Tidy Up the Table	Put trash in trash can	50	50	80
	Put socks in box	60	80	90
	Put marker in pen holder	10	10	30
	Open drawer	20	40	60
	Put lollipop in drawer	10	10	30
	Close drawer	40	60	80
Make Coffee	Turn on coffee machine	100	100	100
	Put funnel onto carafe	0	20	80
	Pour powder into funnel	0	10	10
	Pour water	10	30	70
Avg. Success Rate		30	41	63

Figure 4: **Left:** Real-robot long-horizon tasks. **Right:** Success rate (%) of multi-task agents on real-robot tasks. We collect 8 demonstrations and evaluate 10 episodes for each task.

4.3 Real-Robot Results

To evaluate the effectiveness of SGRv2 in a real-robot setting, we conduct experiments using the Franka Emika Panda across two long-horizon tasks (a total of 10 sub-tasks), and a generalization task. For more details on the robot setup and task designs, please refer to Appendix C.

Long-horizon Tasks. We collect 8 demonstrations per task and train multi-task agents. Each sub-task is tested across 10 episodes. We present comparative results between PerAct, RVT, and SGRv2 in Figure 4, where SGRv2 demonstrates a substantial performance advantage. A common issue with PerAct is that it tends to bias towards occupied voxels, frequently causing collisions. For RVT, typical failures stem from large position errors along the camera’s viewing direction, potentially caused from the inaccuracies in the virtual images rendered orthogonal to the real camera’s perspective.

Generalization Task. We assess the generalization capability of SGRv2 by employing 6 cups of different colors. Each scene involves one target cup and two distractor cups of different colors. We collect 5 demonstrations for each of the 4 colors and test the model on both 4 seen and 2 unseen scenarios. Each color is tested across 10 episodes. As indicated

Method	Seen	Unseen
PerAct	100	10
RVT	100	5
SGRv2 w/o sem.	100	0
SGRv2	100	70

in the right table, compared with PerAct and RVT, SGRv2 exhibits the ability to generalize across color variations. The results show SGRv2 without the semantic branch achieves zero performance on unseen colors, underlining the critical role of semantic awareness in enhancing generalization.

5 Discussion

Limitations. Our models are currently trained using a vanilla BC objective. A promising direction involves integrating the Diffusion Policy [2], which excels in dealing with multimodal and heterogeneous trajectories, with our locality framework to further enhance performance in real world. Additionally, due to our focus on sample efficiency, the evaluations on generalization are currently insufficient. We are eager to expand this work to include a broader range of generalization aspects, such as object shapes, camera positions, and background textures.

Conclusion. We present SGRv2, a systematic framework of visuomotor policy that considers both visual and action representations. Built upon the SGR, SGRv2 integrates action locality across its entire framework. Through comprehensive evaluations across a diverse range of tasks in multiple simulated and real-world environments with limited data availability, SGRv2 exhibits superior performance and outstanding sample efficiency.

References

- [1] B. D. Argall, S. Chernova, M. Veloso, and B. Browning. A survey of robot learning from demonstration. *Robotics and autonomous systems*, 57(5):469–483, 2009.
- [2] C. Chi, S. Feng, Y. Du, Z. Xu, E. Cousineau, B. Burchfiel, and S. Song. Diffusion policy: Visuomotor policy learning via action diffusion. *arXiv preprint arXiv:2303.04137*, 2023.
- [3] T. Z. Zhao, V. Kumar, S. Levine, and C. Finn. Learning fine-grained bimanual manipulation with low-cost hardware. *arXiv preprint arXiv:2304.13705*, 2023.
- [4] Y. LeCun, B. Boser, J. S. Denker, D. Henderson, R. E. Howard, W. Hubbard, and L. D. Jackel. Backpropagation applied to handwritten zip code recognition. *Neural computation*, 1(4):541–551, 1989.
- [5] Z. Liu, H. Mao, C.-Y. Wu, C. Feichtenhofer, T. Darrell, and S. Xie. A convnet for the 2020s. In *Proceedings of the IEEE/CVF conference on computer vision and pattern recognition*, pages 11976–11986, 2022.
- [6] J. L. Elman. Finding structure in time. *Cognitive science*, 14(2):179–211, 1990.
- [7] A. Graves and A. Graves. Long short-term memory. *Supervised sequence labelling with recurrent neural networks*, pages 37–45, 2012.
- [8] Y. J. Ma, S. Sodhani, D. Jayaraman, O. Bastani, V. Kumar, and A. Zhang. Vip: Towards universal visual reward and representation via value-implicit pre-training. *arXiv preprint arXiv:2210.00030*, 2022.
- [9] S. Nair, A. Rajeswaran, V. Kumar, C. Finn, and A. Gupta. R3m: A universal visual representation for robot manipulation. *arXiv preprint arXiv:2203.12601*, 2022.
- [10] T. Zhang, Y. Hu, H. Cui, H. Zhao, and Y. Gao. A universal semantic-geometric representation for robotic manipulation. In *Conference on Robot Learning*, pages 3342–3363. PMLR, 2023.
- [11] Y. Ze, G. Zhang, K. Zhang, C. Hu, M. Wang, and H. Xu. 3d diffusion policy. *arXiv preprint arXiv:2403.03954*, 2024.
- [12] S. James, Z. Ma, D. R. Arrojo, and A. J. Davison. Rlbench: The robot learning benchmark & learning environment. *IEEE Robotics and Automation Letters*, 5(2):3019–3026, 2020.
- [13] J. Gu, F. Xiang, X. Li, Z. Ling, X. Liu, T. Mu, Y. Tang, S. Tao, X. Wei, Y. Yao, et al. Maniskill2: A unified benchmark for generalizable manipulation skills. *arXiv preprint arXiv:2302.04659*, 2023.
- [14] A. Mandlekar, S. Nasiriany, B. Wen, I. Akinola, Y. Narang, L. Fan, Y. Zhu, and D. Fox. Mimicgen: A data generation system for scalable robot learning using human demonstrations. *arXiv preprint arXiv:2310.17596*, 2023.
- [15] G. Qian, Y. Li, H. Peng, J. Mai, H. A. A. K. Hammoud, M. Elhoseiny, and B. Ghanem. Pointnext: Revisiting pointnet++ with improved training and scaling strategies. *arXiv preprint arXiv:2206.04670*, 2022.
- [16] M. Shridhar, L. Manuelli, and D. Fox. Perceiver-actor: A multi-task transformer for robotic manipulation. *arXiv preprint arXiv:2209.05451*, 2022.
- [17] A. Goyal, J. Xu, Y. Guo, V. Blukis, Y.-W. Chao, and D. Fox. Rvt: Robotic view transformer for 3d object manipulation. In *Conference on Robot Learning*, pages 694–710. PMLR, 2023.
- [18] M. Laskin, A. Srinivas, and P. Abbeel. Curl: Contrastive unsupervised representations for reinforcement learning. In *International Conference on Machine Learning*, pages 5639–5650. PMLR, 2020.

- [19] M. Laskin, K. Lee, A. Stooke, L. Pinto, P. Abbeel, and A. Srinivas. Reinforcement learning with augmented data. *Advances in neural information processing systems*, 33:19884–19895, 2020.
- [20] I. Kostrikov, D. Yarats, and R. Fergus. Image augmentation is all you need: Regularizing deep reinforcement learning from pixels. *arXiv preprint arXiv:2004.13649*, 2020.
- [21] C. Gelada, S. Kumar, J. Buckman, O. Nachum, and M. G. Bellemare. Deepmdp: Learning continuous latent space models for representation learning. In *International Conference on Machine Learning*, pages 2170–2179. PMLR, 2019.
- [22] D. Hafner, T. Lillicrap, J. Ba, and M. Norouzi. Dream to control: Learning behaviors by latent imagination. *arXiv preprint arXiv:1912.01603*, 2019.
- [23] R. Jonschkowski and O. Brock. Learning state representations with robotic priors. *Autonomous Robots*, 39:407–428, 2015.
- [24] A. Zhang, R. McAllister, R. Calandra, Y. Gal, and S. Levine. Learning invariant representations for reinforcement learning without reconstruction. *arXiv preprint arXiv:2006.10742*, 2020.
- [25] I. Radosavovic, T. Xiao, S. James, P. Abbeel, J. Malik, and T. Darrell. Real-world robot learning with masked visual pre-training. *arXiv preprint arXiv:2210.03109*, 2022.
- [26] A. Majumdar, K. Yadav, S. Arnaud, Y. J. Ma, C. Chen, S. Silwal, A. Jain, V.-P. Berges, P. Abbeel, J. Malik, et al. Where are we in the search for an artificial visual cortex for embodied intelligence? *arXiv preprint arXiv:2303.18240*, 2023.
- [27] Y. Hu, R. Wang, L. E. Li, and Y. Gao. For pre-trained vision models in motor control, not all policy learning methods are created equal. *arXiv preprint arXiv:2304.04591*, 2023.
- [28] R. Shah and V. Kumar. Rrl: Resnet as representation for reinforcement learning. *arXiv preprint arXiv:2107.03380*, 2021.
- [29] Z. Yuan, Z. Xue, B. Yuan, X. Wang, Y. Wu, Y. Gao, and H. Xu. Pre-trained image encoder for generalizable visual reinforcement learning. *arXiv preprint arXiv:2212.08860*, 2022.
- [30] T. Xiao, I. Radosavovic, T. Darrell, and J. Malik. Masked visual pre-training for motor control. *arXiv preprint arXiv:2203.06173*, 2022.
- [31] S. Parisi, A. Rajeswaran, S. Purushwalkam, and A. Gupta. The unsurprising effectiveness of pre-trained vision models for control. In *International Conference on Machine Learning*, pages 17359–17371. PMLR, 2022.
- [32] S. James, K. Wada, T. Laidlow, and A. J. Davison. Coarse-to-fine q-attention: Efficient learning for visual robotic manipulation via discretisation. In *Proceedings of the IEEE/CVF Conference on Computer Vision and Pattern Recognition*, pages 13739–13748, 2022.
- [33] Y. Ze, G. Yan, Y.-H. Wu, A. Macaluso, Y. Ge, J. Ye, N. Hansen, L. E. Li, and X. Wang. Gnfactor: Multi-task real robot learning with generalizable neural feature fields. In *Conference on Robot Learning*, pages 284–301. PMLR, 2023.
- [34] H. Liu, L. Lee, K. Lee, and P. Abbeel. Instruction-following agents with jointly pre-trained vision-language models. *arXiv preprint arXiv:2210.13431*, 2022.
- [35] P.-L. Guhur, S. Chen, R. Garcia, M. Tapaswi, I. Laptev, and C. Schmid. Instruction-driven history-aware policies for robotic manipulations. *arXiv preprint arXiv:2209.04899*, 2022.
- [36] Y. Seo, J. Kim, S. James, K. Lee, J. Shin, and P. Abbeel. Multi-view masked world models for visual robotic manipulation. *arXiv preprint arXiv:2302.02408*, 2023.

- [37] C. R. Qi, L. Yi, H. Su, and L. J. Guibas. Pointnet++: Deep hierarchical feature learning on point sets in a metric space. *Advances in neural information processing systems*, 30, 2017.
- [38] H.-S. Fang, C. Wang, M. Gou, and C. Lu. Graspnet-1billion: A large-scale benchmark for general object grasping. In *Proceedings of the IEEE/CVF conference on computer vision and pattern recognition*, pages 11444–11453, 2020.
- [39] M. Sundermeyer, A. Mousavian, R. Triebel, and D. Fox. Contact-graspnet: Efficient 6-dof grasp generation in cluttered scenes. In *2021 IEEE International Conference on Robotics and Automation (ICRA)*, pages 13438–13444. IEEE, 2021.
- [40] W. Huang, I. Mordatch, P. Abbeel, and D. Pathak. Generalization in dexterous manipulation via geometry-aware multi-task learning. *arXiv preprint arXiv:2111.03062*, 2021.
- [41] Y.-H. Wu, J. Wang, and X. Wang. Learning generalizable dexterous manipulation from human grasp affordance. *arXiv preprint arXiv:2204.02320*, 2022.
- [42] Y. Qin, B. Huang, Z.-H. Yin, H. Su, and X. Wang. Dexpoint: Generalizable point cloud reinforcement learning for sim-to-real dexterous manipulation. *arXiv preprint arXiv:2211.09423*, 2022.
- [43] M. Liu, X. Li, Z. Ling, Y. Li, and H. Su. Frame mining: a free lunch for learning robotic manipulation from 3d point clouds. *arXiv preprint arXiv:2210.07442*, 2022.
- [44] T. Gervet, Z. Xian, N. Gkanatsios, and K. Fragkiadaki. Act3d: 3d feature field transformers for multi-task robotic manipulation. In *7th Annual Conference on Robot Learning*, 2023.
- [45] S. Chen, R. Garcia, I. Laptev, and C. Schmid. Sugar: Pre-training 3d visual representations for robotics. *arXiv preprint arXiv:2404.01491*, 2024.
- [46] T.-W. Ke, N. Gkanatsios, and K. Fragkiadaki. 3d diffuser actor: Policy diffusion with 3d scene representations. *arXiv preprint arXiv:2402.10885*, 2024.
- [47] Z. Xue, Z. Yuan, J. Wang, X. Wang, Y. Gao, and H. Xu. Useek: Unsupervised se (3)-equivariant 3d keypoints for generalizable manipulation. In *2023 IEEE International Conference on Robotics and Automation (ICRA)*, pages 1715–1722. IEEE, 2023.
- [48] H. Ryu, H.-i. Lee, J.-H. Lee, and J. Choi. Equivariant descriptor fields: Se (3)-equivariant energy-based models for end-to-end visual robotic manipulation learning. *arXiv preprint arXiv:2206.08321*, 2022.
- [49] A. Simeonov, Y. Du, A. Tagliasacchi, J. B. Tenenbaum, A. Rodriguez, P. Agrawal, and V. Sitzmann. Neural descriptor fields: Se (3)-equivariant object representations for manipulation. In *2022 International Conference on Robotics and Automation (ICRA)*, pages 6394–6400. IEEE, 2022.
- [50] J. Yang, C. Deng, J. Wu, R. Antonova, L. Guibas, and J. Bohg. Equivact: Sim (3)-equivariant visuomotor policies beyond rigid object manipulation. *arXiv preprint arXiv:2310.16050*, 2023.
- [51] E. Chun, Y. Du, A. Simeonov, T. Lozano-Perez, and L. Kaelbling. Local neural descriptor fields: Locally conditioned object representations for manipulation. In *2023 IEEE International Conference on Robotics and Automation (ICRA)*, pages 1830–1836. IEEE, 2023.
- [52] C. Gao, Z. Xue, S. Deng, T. Liang, S. Yang, L. Shao, and H. Xu. Riemann: Near real-time se (3)-equivariant robot manipulation without point cloud segmentation. *arXiv preprint arXiv:2403.19460*, 2024.
- [53] F. Fuchs, D. Worrall, V. Fischer, and M. Welling. Se (3)-transformers: 3d roto-translation equivariant attention networks. *Advances in neural information processing systems*, 33:1970–1981, 2020.

- [54] A. Zeng, P. Florence, J. Tompson, S. Welker, J. Chien, M. Attarian, T. Armstrong, I. Krasin, D. Duong, V. Sindhwani, et al. Transporter networks: Rearranging the visual world for robotic manipulation. In *Conference on Robot Learning*, pages 726–747. PMLR, 2021.
- [55] C. R. Qi, H. Su, K. Mo, and L. J. Guibas. Pointnet: Deep learning on point sets for 3d classification and segmentation. In *Proceedings of the IEEE conference on computer vision and pattern recognition*, pages 652–660, 2017.
- [56] A. Simeonov, Y. Du, Y.-C. Lin, A. R. Garcia, L. P. Kaelbling, T. Lozano-Pérez, and P. Agrawal. Se (3)-equivariant relational rearrangement with neural descriptor fields. In *Conference on Robot Learning*, pages 835–846. PMLR, 2023.
- [57] A. Radford, J. W. Kim, C. Hallacy, A. Ramesh, G. Goh, S. Agarwal, G. Sastry, A. Askell, P. Mishkin, J. Clark, et al. Learning transferable visual models from natural language supervision. In *International conference on machine learning*, pages 8748–8763. PMLR, 2021.
- [58] L. X. Shi, A. Sharma, T. Z. Zhao, and C. Finn. Waypoint-based imitation learning for robotic manipulation. In *Conference on Robot Learning*, pages 2195–2209. PMLR, 2023.
- [59] Y. Zhu, J. Wong, A. Mandlekar, R. Martín-Martín, A. Joshi, S. Nasiriany, and Y. Zhu. ro-bosuite: A modular simulation framework and benchmark for robot learning. *arXiv preprint arXiv:2009.12293*, 2020.
- [60] N. Hansen, H. Su, and X. Wang. Td-mpc2: Scalable, robust world models for continuous control. *arXiv preprint arXiv:2310.16828*, 2023.
- [61] A. Jaegle, S. Borgeaud, J.-B. Alayrac, C. Doersch, C. Ionescu, D. Ding, S. Koppula, D. Zoran, A. Brock, E. Shelhamer, et al. Perceiver io: A general architecture for structured inputs & outputs. *arXiv preprint arXiv:2107.14795*, 2021.
- [62] B. Calli, A. Singh, A. Walsman, S. Srinivasa, P. Abbeel, and A. M. Dollar. The ycb object and model set: Towards common benchmarks for manipulation research. In *2015 international conference on advanced robotics (ICAR)*, pages 510–517. IEEE, 2015.

A Simulation Task Details



Figure 5: **Simulation Tasks.** Our simulation experiments encompass 26 tasks (1-26) from RL-Bench, 4 tasks (27-37, where 30-37 are 8 different YCB [62] objects of task *PickSingleYCB*) from ManiSkill2, and 7 tasks (38-44) from MimicGen.

Our simulation experiments are conducted on 3 robot learning benchmarks: RL-Bench [12], ManiSkill2 [13], and MimicGen [14]. See Figure 5 for an overview of the simulation tasks. In these

simulations, all cameras have a resolution of 128×128 . In the following, we will provide a detailed examination of tasks from the three benchmarks.

A.1 RL Bench Tasks

We utilize 26 RL Bench tasks, including 8 tasks used in SGR [10] and 18 tasks used in PerAct [16] and RVT [17]. For tasks with multiple variations, we use the first variation. In RL Bench, we use 5 demonstrations per task, unless specified otherwise. Given that SGR and PerAct provide detailed descriptions of these RL Bench tasks, we omit these details here for simplicity.

A.2 ManiSkill2 Tasks

We utilize 4 ManiSkill2 tasks, each described in detail as follows. (1) **Lift Cube**: Pick up a red cube and lift it to a specified height. (2) **Pick Cube**: Pick up a red cube and move it to a target position. (3) **Stack Cube**: Pick up a red cube and place it onto a green cube. (4) **Pick Single YCB**: Pick up a YCB [62] object and move it to the target position. In our experiments, we use 8 YCB objects (excluding those that are too difficult to pick up): *002_master_chef_can*, *004_sugar_box*, *005_tomato_soup_can*, *006_mustard_bottle*, *007_tuna_fish_can*, *008_pudding_box*, *010_potted_meat_can*, *011_banana*. For the first three tasks, we utilize 50 demonstrations per task, while for the last one (*Pick Single YCB*), we employ 50 demonstrations per YCB object.

A.3 MimicGen Tasks

We utilize 7 MimicGen tasks with 50 demonstrations per task, all employing the initial distribution D_1 , which presents a broader and more challenging range. The details are as follows: (1) **Stack**: Stack a red block on a green one. (2) **Stack Three**: Similar to Stack, but with an additional step of stacking a blue block on the red one. (3) **Square**: Pick up a square nut and place it on a peg. (4) **Threading**: Pick up a needle and thread it through a hole in a tripod. (5) **Coffee**: Pick up a coffee pod, insert it into the coffee machine, and close the machine hinge. (6) **Hammer Cleanup**: Open a drawer, pick up a hammer, place it back into the drawer, and close the drawer. (7) **Mug Cleanup**: Similar to Hammer Cleanup, but with a mug.

B SGRv2 Details

B.1 Architecture Details

Input Data. The SGRv2 model takes as input RGB images $\{I_k\}_{k=1}^K$ of size $H \times W$ and corresponding depth images of the same size from multiple camera views. Point clouds are generated from these depth images using known camera extrinsics and intrinsics. A crucial aspect is the alignment of the RGB images with the point clouds, ensuring a precise one-to-one correspondence between elements in the two data forms. For keyframe control, the point cloud is represented in the robot’s base frame. In contrast, for dense control—inspired by FrameMiner [43]—the point cloud is transformed into the end-effector frame to simplify computation and enhance performance.

For keyframe control, the model additionally receives proprioceptive data z , which includes four scalar values: gripper open state, left finger joint position, right finger joint position, and action sequence timestep. In dense control, proprioceptive data is not utilized. Additionally, following SGR [10], if a task comes with language instruction S , this also forms part of the model’s input.

Other Details. Following SGR [10], we use CLIP-ResNet-50 as the image encoder for the semantic branch. For the 3D encoder-decoder, we employ PointNeXt-XL. The output from the encoder-decoder is a point-wise feature, denoted as $f_i^{\text{raw}} \in \mathbb{R}^C$ for the i -th point, where the feature dimension C is 64. We apply a linear layer followed by a ReLU activation to produce a processed point-wise feature f_i , increasing the feature dimension to 256. We then predict the relative position $\Delta p(f_i)$, magnitude $m(f_i)$ (for dense control), rotation $r(f_i)$, gripper open state $o(f_i)$, and collision indicator $c(f_i)$ (for keyframe control) of the i -th point, where $\Delta p, m, r, o, c$ are 3-layer MLPs. Note that when

representing the ground-truth actions as one-hot vectors—such as rotation, gripper open state, and collision indicators in keyframe control—the action predictions correspond to the output probabilities following the softmax layer. Finally, for each action component, we assign a learned weight $w_*(f_i)$ to each point, where w_* represents separate 3-layer MLPs with softmax normalization across the points dimension.

B.2 SGR Details

SGRv2 is built upon SGR [10], which we briefly introduced in Section 3.1. Here, we provide a detailed description of SGR’s three components: semantic branch, geometric branch, and fusion network.

Semantic Branch. Using a collection of RGB images $\{I_k\}_{k=1}^K$ from K calibrated cameras, they initially apply a frozen pre-trained 2D model \mathcal{G} , such as CLIP’s visual encoder, to extract multi-view image features $\{\mathcal{G}(I_k)\}_{k=1}^K$. When a language instruction S accompanies a task, they utilize a pre-trained language model \mathcal{H} , like CLIP’s language encoder, to generate the language features $\mathcal{H}(S)$. They align these image features $\mathcal{G}(I_k)$ with the language features $\mathcal{H}(S)$ using a visual grounding module, producing $\{M_k\}_{k=1}^K$. Subsequently, they rescale the visual or aligned feature maps to the dimensions of the original images through bilinear interpolation and reduce their channels by 1×1 convolution, generating a set of features $\{F_k\}_{k=1}^K$, where each $F_k \in \mathbb{R}^{H \times W \times C_1}$. These high-level semantic features are then back-projected into 3D space to form point-wise features for the point cloud, expressed as $F_{\text{sem}} \in \mathbb{R}^{N \times C_1}$, where $N = K \times H \times W$.

Geometric Branch. They construct the initial point cloud coordinates $P = \{p_i\}_{i=1}^N \in \mathbb{R}^{N \times 3}$ and RGB features $F_c \in \mathbb{R}^{N \times 3}$ using multi-view RGB-D images and camera parameters (i.e., camera intrinsics and extrinsics). Optionally, they append a D -dimensional vector, derived from robot proprioceptive data z via a linear layer, to each point feature. They then process the point cloud coordinates P and features F_c through a hierarchical PointNeXt encoder, extracting compact geometric coordinates $P' \in \mathbb{R}^{M \times 3}$ and features $F'_c \in \mathbb{R}^{M \times C_2}$ ($M < N$).

Fusion Network. To merge the two complementary branches, they first subsample the point-wise semantic features F_{sem} using the same point subsampling procedure as in the geometric branch, resulting in $F'_{\text{sem}} \in \mathbb{R}^{M \times C_1}$. They then perform a channel-wise concatenation of the semantic and geometric features to form $F_{\text{fuse}} = \text{Concat}(F'_{\text{sem}}, F'_c) \in \mathbb{R}^{M \times (C_1 + C_2)}$. Finally, the fused features are processed through several set abstraction blocks [37, 15], enabling a cohesive modeling of the cross-modal interaction between 2D semantics and 3D geometric information.

B.3 Training Details

Losses. As illustrated in Section 3.3, in keyframe control, our loss objective is as follows:

$$\mathcal{L}_{\text{keyframe}} = \alpha_1 \mathcal{L}_{\text{pos}} + \alpha_2 \mathcal{L}_{\text{rot}} + \alpha_3 \mathcal{L}_{\text{open}} + \alpha_4 \mathcal{L}_{\text{collide}}, \quad (3)$$

where \mathcal{L}_{pos} is L1 loss, and \mathcal{L}_{rot} , $\mathcal{L}_{\text{open}}$, and $\mathcal{L}_{\text{collide}}$ are cross-entropy losses. In our experiments, we set $\alpha_1 = 300$ and $\alpha_2 = \alpha_3 = \alpha_4 = 1$.

In dense control, our loss objective is:

$$\mathcal{L}_{\text{dense}} = \beta_1 (\mathcal{L}_{\text{dir}} + \mathcal{L}_{\text{mag}}) + \beta_2 \mathcal{L}_{\text{rot}} + \beta_3 \mathcal{L}_{\text{open}} + \beta_4 \mathcal{L}_{\text{reg}}, \quad (4)$$

where \mathcal{L}_{dir} , \mathcal{L}_{mag} and \mathcal{L}_{rot} are MSE losses, $\mathcal{L}_{\text{open}}$ is cross-entropy loss, and \mathcal{L}_{reg} is smoothness regularization loss. In our experiments, we set $\beta_1 = 10$, $\beta_2 = \beta_3 = 1$ and $\beta_4 = 0.3$.

Data Augmentation. (1) **Translation and rotation perturbations:** in keyframe control, the training samples is augmented with ± 0.125 m translation perturbations and $\pm 45^\circ$ yaw rotation perturbations. (2) **Color drop** is to randomly replace colors with zero values. This technique serves as a powerful augmentation for PointNeXt [15], leading to significant enhancements in the performance of tasks where color information is available. (3) **Feature drop:** Color drop randomly replaces colors with zero values, which results in both the RGB and semantic features becoming constant.

However, there are certain tasks where colors play a crucial role, and disregarding color information in these tasks would make them unsolvable. To address this issue, we propose *feature drop*. Specifically, this involves randomly replacing the semantic features with zero values, while keeping the RGB values unchanged. (4) **Point resampling** is a widely used technique in point cloud data processing that adjusts the density of the point cloud. It involves selecting a subset of points from the original dataset to create a new dataset with a modified density. Firstly, we filter out points outside the workspace. Then in keyframe control, we resample 4096 points from the point cloud using farthest point sampling (FPS), while in dense control, we resample 1200 points using the same method. (5) **Demo augmentation** [32] [16], used in keyframe control, captures transitions from intermediate points along a trajectory to keyframe states, rather than from the initial state to the keyframe state. This approach significantly increases the volume of the training data.

Hyperparameters. The configuration of hyperparameters applied in our studies are shown in Table 4. For each task, the experiments are conducted on a single NVIDIA GeForce RTX 3090 GPU.

Table 4: Hyper-parameters used in our simulation experiments.

Config	Keyframe Control	Dense Control
Training iterations	20,000	100,000
Lerning rate	0.003	0.0003
Batch size	16	16
Optimizer	AdamW	AdamW
Lr Scheduler	Cosine	Cosine
Warmup step	200	0
Weight decay	1×10^{-6}	1×10^{-6}
Color drop	0.4	0
Feature drop	0	0.4
Number of input points	4096	1200

C Real-Robot Details

C.1 Real-Robot Setup

For our real-robot experiments, we use a Franka Emika Panda manipulator equipped with a parallel gripper. We utilize keyframe control, and the motion planning is executed through MoveIt³. Perception is achieved through an Intel RealSense L515 camera, positioned in front of the scene. The camera generates RGB-D images with a resolution of 1280×720 . We leverage the `realsense-ros`⁴ to align depth images with color images. The extrinsic calibration between the camera frame and robot base frame is carried out using the MoveIt calibration package.

When preprocessing the RGB-D images, we resize the 1280×720 images to 256×256 using nearest-neighbor interpolation. We choose this interpolation method instead of others, like bilinear interpolation, because the latter can introduce artifacts into the depth map, resulting in a noisy point cloud. Following these steps enables us to process RGB-D images as we do in our simulation experiments. It is essential to adjust the camera’s intrinsic parameters appropriately after resizing the images. We train SGRv2 for 40,000 training steps and use the final checkpoint for evaluation.

C.2 Real-Robot Tasks

Our real-robot experiments involve three tasks: Tidy Up the Table, Make Coffee, and Move Color Cup to Target. The first two are long-horizon tasks, while the last is a generalization task. We provide details of the task design as follows.

Tidy Up the Table (as shown in Figure 4 Top Left) is to place the clutter on the table in its appropriate locations. The task consists of 6 sub-tasks, each detailed as follows: (1) *Put trash in trash*

³<https://moveit.ros.org/>

⁴<https://github.com/IntelRealSense/realsense-ros>

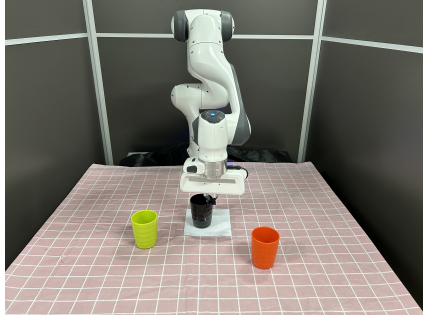


Figure 6: Real-robot generalization task.

Method	Avg. Success \uparrow	Open Microwave	Open Door	Water Plants	Toilet Seat Up	Phone On Base	Put Books	Take Out Umbrella	Open Fridge
R3M	4.7	0.9 \pm 0.6	36.4 \pm 3.7	2.9 \pm 3.7	15.5 \pm 2.1	0.0 \pm 0.0	0.5 \pm 0.9	5.2 \pm 8.7	3.2 \pm 1.4
PointNeXt	25.3	7.1 \pm 6.3	60.9 \pm 5.2	5.6 \pm 4.6	49.9 \pm 14.7	46.4 \pm 4.9	57.5 \pm 8.2	37.5 \pm 2.3	9.2 \pm 4.0
PerAct	22.3	4.3 \pm 7.0	59.6 \pm 16.0	28.5 \pm 3.1	69.3 \pm 11.1	0.0 \pm 0.0	25.1 \pm 4.4	75.9 \pm 7.0	3.1 \pm 1.3
SGR	23.6	6.4 \pm 2.2	55.3 \pm 3.7	24.9 \pm 8.2	30.7 \pm 9.2	47.2 \pm 1.4	29.3 \pm 5.2	36.3 \pm 6.4	7.1 \pm 1.5
RVT	40.4	18.3 \pm 1.8	71.2 \pm 2.8	34.8 \pm 3.3	47.6 \pm 6.7	62.3 \pm 1.4	46.5 \pm 10.9	85.3 \pm 4.5	24.0 \pm 4.2
SGRv2 (ours)	53.2	27.2 \pm 2.0	76.8 \pm 8.0	38.0 \pm 1.7	89.6 \pm 2.8	84.1 \pm 4.5	63.7 \pm 11.8	74.5 \pm 5.5	13.2 \pm 3.4
Method	Open Drawer	Slide Block	Sweep To Dustpan	Meat Off Grill	Turn Tap	Put In Drawer	Close Jar	Drag Stick	Stack Blocks
R3M	0.0 \pm 0.0	24.0 \pm 8.8	0.4 \pm 0.4	0.1 \pm 0.2	26.1 \pm 7.2	0.0 \pm 0.0	0.0 \pm 0.0	0.3 \pm 0.5	0.0 \pm 0.0
PointNeXt	21.7 \pm 20.4	59.5 \pm 22.1	42.0 \pm 34.7	59.9 \pm 17.8	48.7 \pm 13.4	17.1 \pm 27.8	36.0 \pm 4.6	18.5 \pm 32.1	1.9 \pm 1.6
PerAct	56.4 \pm 18.0	47.5 \pm 24.3	2.8 \pm 0.4	85.9 \pm 6.9	8.0 \pm 7.5	0.1 \pm 0.2	0.5 \pm 0.6	10.3 \pm 6.4	1.7 \pm 0.6
SGR	31.9 \pm 6.2	72.0 \pm 27.1	43.6 \pm 8.4	52.7 \pm 5.1	34.4 \pm 7.4	8.3 \pm 9.2	13.3 \pm 5.6	64.4 \pm 11.4	0.0 \pm 0.0
RVT	75.1 \pm 2.6	85.1 \pm 2.2	19.6 \pm 17.4	90.5 \pm 2.2	38.4 \pm 5.4	19.6 \pm 5.5	25.2 \pm 3.6	45.7 \pm 10.9	8.8 \pm 4.2
SGRv2 (ours)	81.3 \pm 3.1	100.0 \pm 0.0	61.5 \pm 7.2	96.5 \pm 3.9	87.9 \pm 6.9	75.9 \pm 3.6	25.6 \pm 2.2	94.9 \pm 0.6	17.5 \pm 3.0
Method	Screw Bulb	Put In Safe	Place Wine	Put In Cupboard	Sort Shape	Push Buttons	Insert Peg	Stack Cups	Place Cups
R3M	0.0 \pm 0.0	0.3 \pm 0.2	0.4 \pm 0.4	0.0 \pm 0.0	0.0 \pm 0.0	6.8 \pm 3.7	0.0 \pm 0.0	0.0 \pm 0.0	0.0 \pm 0.0
PointNeXt	4.1 \pm 1.5	12.1 \pm 4.2	31.5 \pm 4.5	3.3 \pm 0.6	0.4 \pm 0.4	22.0 \pm 38.1	0.1 \pm 0.2	4.4 \pm 3.8	0.4 \pm 0.4
PerAct	4.4 \pm 5.2	0.9 \pm 0.9	8.7 \pm 1.7	0.4 \pm 0.0	0.4 \pm 0.4	83.1 \pm 5.3	1.9 \pm 1.2	0.1 \pm 0.2	0.7 \pm 0.6
SGR	0.9 \pm 0.8	16.9 \pm 2.2	24.7 \pm 5.8	0.1 \pm 0.2	0.1 \pm 0.2	12.0 \pm 1.4	0.1 \pm 0.2	0.0 \pm 0.0	1.1 \pm 0.9
RVT	24.0 \pm 3.8	30.7 \pm 4.9	92.7 \pm 0.6	5.6 \pm 2.1	1.6 \pm 0.7	90.4 \pm 2.9	4.0 \pm 0.0	3.1 \pm 0.6	1.2 \pm 0.7
SGRv2 (ours)	24.1 \pm 0.6	55.6 \pm 8.0	53.1 \pm 7.4	20.3 \pm 9.2	1.9 \pm 0.6	93.2 \pm 5.3	4.1 \pm 1.4	21.3 \pm 11.8	1.6 \pm 0.7

Table 5: RL Bench results (%) on 5 demonstrations with mean and standard deviation.

can: Pick up the trash and place it in the trash can. (2) *Put socks in box*: Pick up the socks and place them in the box. (3) *Put marker in pen holder*: Pick up the marker and place it in the pen holder. (4) *Open drawer*: Grasp the drawer handle and pull it open. (5) *Put lollipop in drawer*: Pick up the lollipop and place it into the drawer. (6) *Close drawer*: Push the drawer closed.

Make Coffee (as shown in Figure 4 Bottom Left) is to make pour-over coffee. This task is composed of 4 sub-tasks, each described in detail as follows: (1) *Turn on coffee machine*: Press the button on the coffee machine to activate it. (2) *Put funnel onto carafe*: Pick up the funnel and place it onto the carafe. (3) *Pour powder into funnel*: Pick up the powder holder and pour the powder into the funnel. (4) *Pour water*: Pick up the kettle and pour the water onto the powder in the funnel.

Move Color Cup to Target (as shown in Figure 6) is to select the target color cup from three cups and move it to the white area. The target color is indicated through language instructions. We have 6 cups of different colors: *white, red, yellow, orange, black, and green*. Each scenario involves one target cup and two distractor cups of different colors. We collect five demonstrations for each of the first 4 colors and test the model on both 4 seen and 2 unseen scenarios.

Method	Avg. Success \uparrow	Avg. Rank \downarrow	LiftCube	PickCube	StackCube	PickSingleYCB
PointNeXt	16.8	2.5	50.8 \pm 15.2	4.7 \pm 0.4	10.6 \pm 4.3	1.1 \pm 0.1
SGR	14.9	2.5	26.9 \pm 4.0	12.2 \pm 3.1	3.5 \pm 2.2	17.0 \pm 0.2
SGRv2 (ours)	55.8	1.0	80.5 \pm 7.3	72.9 \pm 4.1	27.7 \pm 4.3	42.2 \pm 2.3

Method	Avg. Success \uparrow	Avg. Rank \downarrow	Stack	StackThree	Square	Threading	Coffee	HammerCleanup	MugCleanup
PointNeXt	13.6	2.9	56.1 \pm 6.4	3.7 \pm 1.4	0.9 \pm 0.5	3.6 \pm 2.2	12.0 \pm 5.2	11.7 \pm 2.8	7.1 \pm 0.9
SGR	14.2	2.0	50.8 \pm 7.7	5.6 \pm 1.7	1.3 \pm 0.5	4.0 \pm 0.8	14.1 \pm 2.0	14.1 \pm 1.7	9.7 \pm 2.4
SGRv2 (ours)	26.0	1.0	81.2 \pm 4.4	37.9 \pm 1.5	2.8 \pm 0.7	6.7 \pm 2.0	27.9 \pm 7.0	16.1 \pm 3.9	9.7 \pm 2.7

Table 6: ManiSkill2 and MimicGen results (%) on 50 demonstrations with mean and standard deviation.

Method	Avg. Success \uparrow	Open Microwave	Open Door	Water Plants	Toilet Seat Up	Phone On Base	Put Books	Take Out Umbrella	Open Fridge
SGRv2	53.2	27.2	76.8	38.0	89.6	84.1	63.7	74.5	13.2
SGRv2 w/o decoder	21.3	4.4	68.4	12.4	38.8	32.8	27.2	35.6	6.8
SGRv2 w/ absolute pos prediction	21.0	8.0	57.6	21.2	17.2	14.8	21.2	44.4	4.4
SGRv2 w/ uniform point weight	44.2	21.6	82.4	28.8	32.0	60.4	68.0	44.0	14.0
SGRv2 w/o dense supervision	40.0	6.4	59.2	6.8	54.4	78.4	60.8	68.0	6.0

Method	Open Drawer	Slide Block	Sweep To Dustpan	Meat Off Grill	Turn Tap	Put In Drawer	Close Jar	Drag Stick	Stack Blocks
SGRv2	81.3	100.0	61.5	96.5	87.9	75.9	25.6	94.9	17.5
SGRv2 w/o decoder	14.0	78.8	15.6	40.8	46.8	4.0	18.8	0.8	0.0
SGRv2 w/ absolute pos prediction	20.4	99.2	50.8	10.8	68.8	4.0	6.4	54.8	1.2
SGRv2 w/ uniform point weight	92.8	100.0	72.8	90.8	67.6	74.0	43.6	97.6	1.6
SGRv2 w/o dense supervision	75.2	92.8	19.2	72.0	84.0	42.0	28.8	59.6	43.2

Method	Screw Bulb	Put In Safe	Place Wine	Put In Cupboard	Sort Shape	Push Buttons	Insert Peg	Stack Cups	Place Cups
SGRv2	24.1	55.6	53.1	20.3	1.9	93.2	4.1	21.3	1.6
SGRv2 w/o decoder	3.2	16.4	27.6	0.0	0.0	56.8	0.4	0.8	1.6
SGRv2 w/ absolute pos prediction	0.4	1.6	3.2	0.0	0.0	35.2	1.6	0.0	0.0
SGRv2 w/ uniform point weight	1.6	32.8	50.4	1.2	0.8	64.4	0.0	5.2	0.8
SGRv2 w/o dense supervision	0.0	30.4	52.0	0.4	0.0	100.0	0.0	0.0	2.4

Table 7: Ablations results (%) for SGRv2 on RLbench with metrics for each task.

D Additional Results

For our simulation experiments using the SGRv2 on RLbench with 5 demonstrations (mentioned in Table 1) and on ManiSkill2 and MimicGen with 50 demonstrations (mentioned in Table 2), we employed 3 random seeds to ensure the reliability of our results. In the main body of the paper, we present averaged results for clarity. Here we include both the mean and standard deviation derived from our simulation results. The results for RLbench are shown in Table 5, and the results for ManiSkill2 and MimicGen are presented in Table 6.

We also report the ablations mentioned in Table 3 for each task in Table 7.